

One-shot ultraspectral imaging with reconfigurable metasurfaces

Author list: Xusheng Cai#, Jian Xiong#, Kaiyu Cui#*, Yidong Huang*, Hongbo Zhu, Zekun Zheng, Sheng Xu, Yuhan He, Fang Liu, Xue Feng, and Wei Zhang

These authors contributed equally to this work

* Corresponding author: kaiyucui@tsinghua.edu.cn; yidonghuang@tsinghua.edu.cn

Affiliation: Department of Electronic Engineering, Beijing National Research Center for Information Science and Technology (BNRist) Tsinghua University, Beijing 100084, China

One-shot spectral imaging that can obtain spectral information from thousands of different points in space at one time has always been difficult to achieve. Its realization makes it possible to get spatial real-time dynamic spectral information, which is extremely important for both fundamental scientific research and various practical applications¹⁻³. In this study, a one-shot ultraspectral imaging device fitting thousands of micro-spectrometers (6336 pixels) on a chip no larger than 0.5 cm², is proposed and demonstrated. Exotic light modulation is achieved by using a unique reconfigurable metasurface supercell with 158400 metasurface units, which enables 6336 micro-spectrometers with dynamic image-adaptive performances to simultaneously guarantee the density of spectral pixels and the quality of spectral reconstruction. Additionally, by constructing a new algorithm based on compressive sensing, the snapshot device can reconstruct ultraspectral imaging information ($\Delta\lambda/\lambda\sim 0.001$) covering a broad (300-nm-wide) visible spectrum with an ultra-high center-wavelength accuracy of 0.04-nm standard deviation and spectral resolution of 0.8 nm. This scheme of reconfigurable metasurfaces makes the device can be directly extended to almost any commercial camera with different spectral bands to seamlessly switch the information between image and spectral image, and will open up a new space for the application of spectral analysis combining with image recognition and intellisense.

Spectral imaging technology can be used to capture spectral information for all points in the field of view^{1,4}. This development trend of spectral analysis technology is indispensable in many areas, including but not limited to environmental monitoring⁵, medicine diagnoses, mineral resource exploration⁶, fine agriculture⁷, astronomy⁸, and so on. So far, spectral imaging only can be got by spatial or temporal scanning⁹⁻¹⁴ and spatial real-time dynamic spectral information cannot be captured. One-shot spectral imaging by integrating thousands of spectrometers to work together is unachievable for current spectrometers due to their complex structure and large volume. Therefore, much effort continues to be invested in the integrated micro-spectrometers using micro-nano filters instead of traditional spectroscopic techniques. There are two main types of micro-nano filters: resonant filters and broadband filters. Resonant filters, such as micro-ring resonators¹⁵⁻¹⁷, optical microcavities^{18,19}, and resonant metasurface structures²⁰⁻²², enable spectral analysis by separately filtering light of different wavelengths and offer relative high spectral resolution. However, it is difficult to simultaneously produce a broad spectrum and high resolution because the number of spectral channels corresponds to the number of filters used. On the other hand, broadband filters, such as quantum dot arrays², photonic crystal plate arrays^{23,24}, disordered scattering structures²⁵, and nanowires with tuneable band gaps³, encode the spectral information of incident light into the response of a set of filters at different detector positions, and a computational spectral algorithm is used to reconstruct the incident spectrum^{2,3,23-27}. This approach can save the number of filters and enable a broad-spectrum reconstruction. Even though there are reports on these types of micro-spectrometers, one-shot spectral imaging has not been realized so far. The huge obstacle is how to get enough spatial resolution to form a spectral image. In this case, each micro-spectrometer with a group of filters operators as a pixel and the number of the micro-spectrometers decides the density of the spectral pixels, namely spatial resolution. Furthermore, how to adapt the ever-changing captured image is another critical issue for getting spatial real-time dynamic spectral information.

In this work, we propose and demonstrate a one-shot spectral imaging device with both ultra-high spectral and spatial resolutions, namely an ultraspectral camera, in a

broad visible light region. The proposed device is based on a reconfigurable metasurface supercell, which consists of 158400 metasurface units (400 metasurface units with different patterns make up a group and 396 groups are arrayed as 18×22 , See details in Supplementary S1), and operates as image-adaptive broadband filters to realize exotic light modulation for thousands of micro-spectrometers simultaneously with a very compact size. Spectral imaging is realized by integrating this reconfigurable metasurface supercell on top of a CMOS image sensor (CIS) and dynamically combining the metasurface units to form thousands of micro-spectrometers (Fig1 a). The effect of the number of metasurface units (N) in a single micro-spectrometer on the fidelity of the reconstructed spectra is investigated. We prove that the incident light can be modulated with a high degree of freedom by reconfigurable metasurface supercell with dramatic changes of transmitted light intensities (Fig1 b-c, See Supplementary Material S1 for more details), while only a small number of metasurface units ($N=25$ per micro-spectrometer as schematically shown in Fig.1b) is enough for spectral imaging in practice. The output signals from the different modulation regions are collected by the CIS chip and then processed to reconstruct the incident spectrum by grafting the algorithm of compressive sensing. Based on this unique working principle, the proposed ultraspectral imaging is able to generate highly accurate spectra of all the pixels in the field of view to form spectral images in one measurement (Fig. 1d), and avoids the need for complex scanning operations (by micro-mechanical structures)⁹⁻¹¹ or switching filters¹²⁻¹⁴, so that a real-time dynamic spectral imaging with high accuracy and resolution is acquirable. In our study, the proposed device could capture a spectral image with more than 6336 pixels (88×72 pixels) in a single shot; in particular, each pixel (micro-spectrometer) could reconstruct the spectrum over a wavelength range of 300nm with a center-wavelength accuracy of 0.04-nm standard deviation and spectral resolution of 0.8 nm. Furthermore, ultraspectral imaging with $\Delta\lambda/\lambda \sim 0.001$ is demonstrated in visible region (λ : 450-750 nm) using a very narrow resolving band of $\Delta\lambda=0.5$ nm. Here, completely polarization-independent performance is realized due to the C_4 symmetric metasurface design (Supplementary S2), which considerably expands the range of applications for this type of micro-spectrometer, as well as spectral imaging.

While, to meet the specialized requirements of polarization applications, a polarizer can be added to the proposed device to easily transform its operation into polarization spectral imaging.

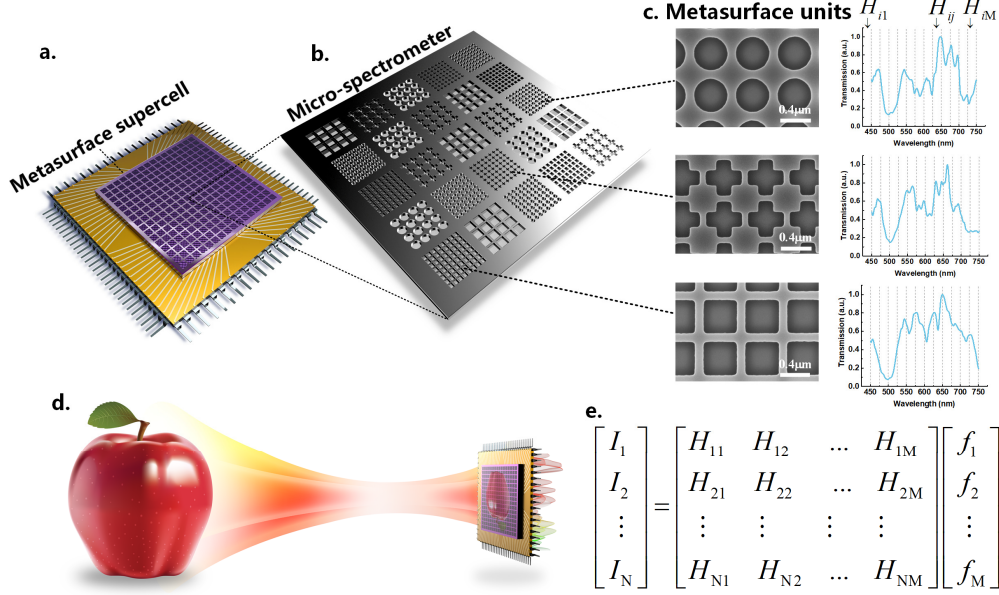


Figure 1 Operation of the proposed ultraspectral imaging device. **a**, The device is composed of a reconfigurable metasurface supercell and a commercial CMOS image sensor (CIS) chip (Thorlab DCC3260M), which forms thousands of micro-spectrometers. During the spectral reconstruction of an object, the adjacent metasurface units in the metasurface supercell are dynamically combined into a reconfigurable and independent micro-spectrometer. **b**, Schematic of a single micro-spectrometer operating as an individual spectral pixel of the device, the metasurface units are reconfigurable with number (N) between 20 and 400. **c**, Three scanning electron microscopy (SEM) images of selected metasurface units with C_4 symmetry. The corresponding modified transmission spectral curve $H_i(\lambda)$ is characterized using a monochromator for calibration. **d**, Snapshot spectral imaging. The light of the object to be imaged is incident on the metasurface supercell first. Then, the difference in the light modulation at various positions alters the measurement result recorded by the CIS chip placed below. Thus, the algorithm of compressive sensing can reconstruct ultraspectral information for all the pixels in an image with a single snapshot. **e**, Matrix equation for computational spectral reconstruction, where I_i is the intensity of the modulated light below the i -th metasurface unit detected by the CIS. $f(\lambda)$ is the test spectrum of the incident light with M bands.

The design patterns for the metasurface supercell are first formed via electron beam lithography on a silicon-on-insulator (SOI) chip with a 220-nm-thick silicon layer; these patterns are then transferred onto the silicon layer by inductively coupled plasma etching. After that, the middle silicon dioxide layer is removed through wet etching with buffered hydrofluoric acid, thereby suspending the metasurface supercell. Finally, the top silicon layer of the SOI consisting of the suspended metasurface supercell is entirely transferred on top of a CIS chip using the polydimethylsiloxane (PDMS) transfer approach (See details in Supplementary S3). Obviously, the proposed device can be fabricated entirely using CMOS-compatible processing technology, which enables low-cost mass production.

Modulated incident light is absorbed by the underlying CIS chip, which converts the optical signals to electrical signals. An algorithm is then applied to process the electrical data and reconstruct the incident spectrum. As the spectral imaging device is comprised of thousands of micro-spectrometers, here, we describe the working principle of a single micro-spectrometer. The transmission response of the i -th metasurface unit is denoted as $h_i(\lambda)$, $i = 1, 2, 3, \dots, N$, where N is the number of the units in a single spectrometer, λ is the wavelength, and the incident spectrum to be measured is denoted as $f(\lambda)$. Then, the signal intensity I_i received by the CIS below the i -th metasurface unit is as follows:

$$I_i = \int_{\lambda_1}^{\lambda_2} f(\lambda) h_i(\lambda) R(\lambda) P(\lambda) d\lambda, \quad (1)$$

where $R(\lambda)$ is the absorption quantum efficiency of the CIS for wavelength λ , $P(\lambda)$ is the dispersion curve of the lens imaging system, and λ_1 and λ_2 are the lower and upper limits of the incident spectral distribution, respectively.

Here, we set $H_i(\lambda) = h_i(\lambda) R(\lambda) P(\lambda)$, which is the modified transmission spectral curve and can be predetermined via measurement (Fig. 1c, for more information about measured curves, see Supplementary S1). Accordingly, the signal intensity equation can be simplified as follows:

$$I_i = \int_{\lambda_1}^{\lambda_2} f(\lambda) H_i(\lambda) d\lambda, \quad (2)$$

where the integral equations are discretized to produce a matrix equation as shown in Fig. 1e. In principle, the spectrum I_i can be directly reconstructed via matrix inversion if a sufficient number of equations are available. However, in practice, N is typically smaller than the number of spectral sampling points M in order to reduce the size of a single micro-spectrometer. Thus, a unique solution for the matrix cannot be obtained. In addition, even if N could be increased such that the matrix satisfies the inversion condition, errors would still occur in the value I_i measured by the CIS chip as well as the calibration value $H_i(\lambda)$ of the transmission spectral curve. Therefore, the original spectrum cannot be accurately reconstructed by directly solving the matrix equation shown in Fig.1e. In this study, grafting the algorithm of compressive sensing, dictionary learning based on sparse coding²⁸⁻³⁰ is used to recreate the original spectrum (see Supplementary S4).

To illustrate the performance of ultraspectral imaging, Fig. 2 presents measurements of monochromatic light sources over a spectral range of 450-750 nm with $N=25$. In particular, Fig. 2a shows a comparison of the reconstructed monochromatic light obtained using a single micro-spectrometer of the proposed device (blue line) with that obtained using a commercial spectrometer (black dashed line, OceanView QE Pro). As can be seen from Fig. 2b, the center-wavelength accuracy of the monochromatic light is as high as 0.04 nm, which is a standard deviation of the reconstruction error compared with the referenced commercial spectrometer.

Another important performance indicator of a micro-spectrometer is its resolving performance for two monochromatic lights with very similar wavelengths. By using an adaptive band method to balance the conflicting requirements of spectral resolution and spectral width, it is possible to provide denser sampling points and higher resolution for reconstructing ultra-fine spectral lines. To demonstrate this, an experiment is conducted wherein a pair of peaks is formed by using the 546-nm line of a mercury lamp and a tuneable monochromatic light source. To resolve such ultra-fine spectral lines, we

reduce the sampling interval to 0.2 nm and limit the spectral band to within 2 nm (544.6-546.6 nm). As shown in Fig. 2c, using the adaptive band method, the micro-spectrometer effectively resolves the abovementioned double peaks with a wavelength interval of only 0.8 nm. Here, the linewidths of the reconstructed double peaks (blue curves) are broadened to only 0.23 nm and 0.24 nm. To the best of our knowledge, this double-peak resolution is the best result obtained for an on-chip micro-spectrometer, and is approximately an order of magnitude higher than that obtained using a nanowire spectrometer³ (15 nm); in addition, it surpasses the results obtained using commercial portable spectrometers (approximately 2 nm, OceanView QE Pro).

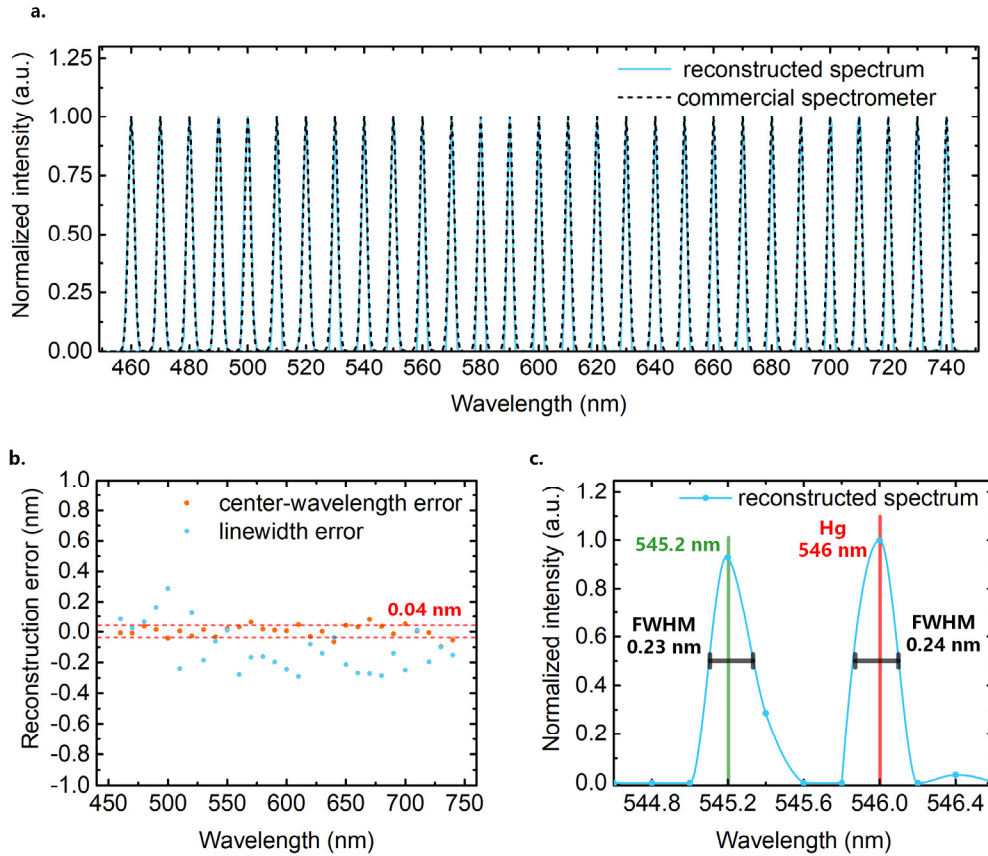


Figure 2 Spectral reconstruction of monochromatic light sources with $N=25$. **a**, Reconstruction results of narrow-spectrum light obtained using a micro-spectrometer of the proposed device (blue line) and those using a commercial spectrometer, namely OceanView QE Pro (black dashed line). **b**, Errors in narrow-spectrum light reconstruction. Here, the Gaussian envelope for the narrow-spectrum light is assumed to estimate linewidth and center-wavelength. **c**, Reconstruction of double peaks corresponding to the 546-nm spectral line of a mercury lamp and 545.2-nm spectral line of a

tunable monochromatic light source; the interval between the two spectral lines is 0.8 nm, while the other spectral lines of the mercury lamp are removed using filters during measurements.

In the visible light region, the proposed ultraspectral imaging device can accurately reconstruct both monochromatic light and complex broad-spectrum signals. Figure 3 shows the reconstruction results for several types of broad spectra. The blue curve is obtained using the micro-spectrometer of the proposed device, while the red curve is obtained using a commercial spectrometer and serves as a reference spectrum. The concept of fidelity is introduced to quantitatively compare the original and the reconstructed spectra:

$$F(X, Y) = \left(\sum_m \sqrt{p_m q_m} \right)^2, \quad (3)$$

where X and Y represent the normalized original spectrum and reconstructed spectrum, respectively, and p_m and q_m are the corresponding intensities at the m -th wavelength sampling point. The fidelities of the broad-spectrum reconstruction results obtained in this experiment are all above 98% even with a small number of metasurface units $N=25$ (Fig. 3a-c), thus demonstrating the good reconstruction ability of the proposed device.

To evaluate the spatial pixel reconstruction ability of the proposed device based on the reconfigurable metasurface supercell, the effect of the number of metasurface units (N) in a single micro-spectrometer on the fidelity of the reconstructed spectra is investigated, where the N units are randomly selected from 158400 metasurface units with 400 different patterns; these evaluation results are shown in Fig. 3d. The error bars in Fig. 3d represent the variance of the reconstruction fidelity obtained for multiple possible random combinations for each N value. As N increases, the reconstruction error gradually decreases, while the value of fidelity gradually improves. This trend can be explained by considering that increasing N reduces the randomness of the solution to the matrix equation in Fig. 1e, thus makes the reconstruction process relatively more robust. For a single micro-spectrometer in the proposed device, N can be dynamically adjusted based on the reconfigurable metasurface supercell considering the noise level

to achieve an optimal trade-off between the pixel density and reconstruction quality of a reconstructed spectra, i.e. a small N and large spectral pixel density could be used at low noise levels, whereas a large N , but with degraded spectral pixel density, could be used at high noise levels. Moreover, for common spectra without intricate information, such as in the case shown in Fig. 3b, high fidelity can still be realized with N as low as 20.

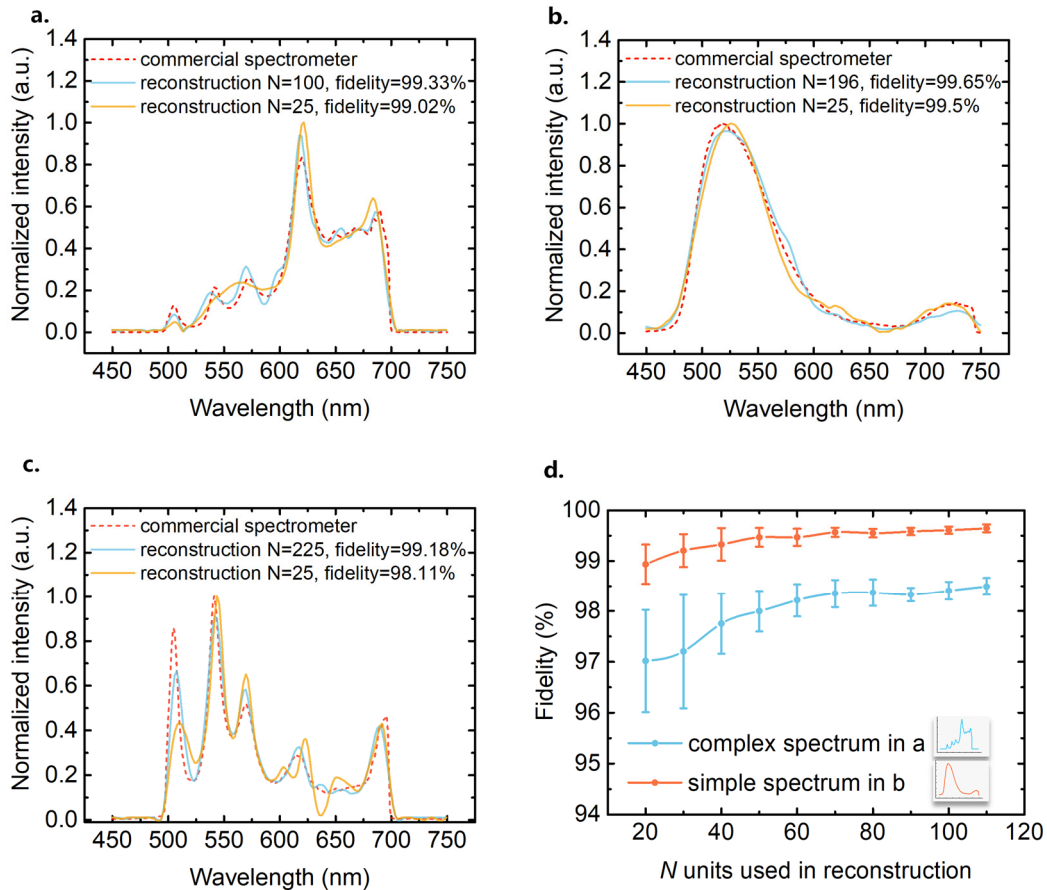


Figure 3 a, b, c Reconstruction results of three broad spectra obtained using a micro-spectrometer of the proposed device (blue curve and yellow curve with different metasurface units N). The spectra detected by a commercial spectrometer are also shown as reference (red dot-curve). Fidelities for the three different spectra are all above 98% even with a small number of metasurface units $N=25$, indicating high consistency between reconstructed and reference spectra. **d**, Spectrum-reconstruction fidelity of a micro-spectrometer with different unit number N . Error bars represent the variance in fidelity obtained by randomly selecting N units from 158400 metasurface units with 400 different patterns. Here, the fidelities of the reconstructed spectra shown in Figs. 3a and b are calculated as examples for a complex and simple spectrum, respectively. It can be observed that for

a small N , fidelity is relatively with high random, but still show a good reconstruction results with fidelity larger than 96%; as N increases, average fidelity gradually increases, and variance clearly decreases, which is in agreement with theoretical analysis.

Finally, we implemented ultraspectral imaging ($\Delta\lambda/\lambda\sim 0.001$) with the reconfigurable metasurface supercell on top of a CIS, as shown in Fig. 4b. Figure 4a shows the ultraspectral imaging results for a plate of fruits under light from a fluorescent lamp. Here, the ordinary color image of the fruits and the metasurface modulated image are both shown in Fig. 4a, where the pattern of 6336 micro-spectrometers can be loomed in the latter one. Ultraspectral information over a spectral range of 450-750 nm at a 0.5-nm sampling interval can be obtained by a snapshot fashion for all points in the field of view using 601 wavelength bands. To visualize the spectrum information with high spatial resolution (601 bands \times 6336 pixels), we convert the spectrum data to a post-colored spectral image and a data cube, wherein spectral images at five single-wavelength of 510 nm, 540 nm, 570 nm, 600 nm, and 630 nm are selected from 601 wavelength bands as examples and presented in Fig. 4a. It should be noted that the data cube (601 \times 6336) is obtained in a snapshot manner rather than using the conventional method of spatial scanning or spectral filters with several bands. Figure 4c shows the spectral reconstruction results for different fruits at selected image positions indicated in Fig. 4a. Because no currently available commercial spectral imaging device can achieve similar functionality, no spectral reference curves of the corresponding objects are provided in Fig. 4c. Furthermore, using reconfigurable spectra pixels with an image recognition technique, the proposed ultraspectral imaging device can be used to generate any pattern of spectral reconstruction units locally and prevent jagged edges resulting from low pixel density in spectral imaging, which would be of considerable significance in image recognition applications. In addition, as demonstrated via our experiment, good reconstruction is possible even with an ordinary light source in our experiment, which is considerably important for in situ exploration and remote sensing applications.

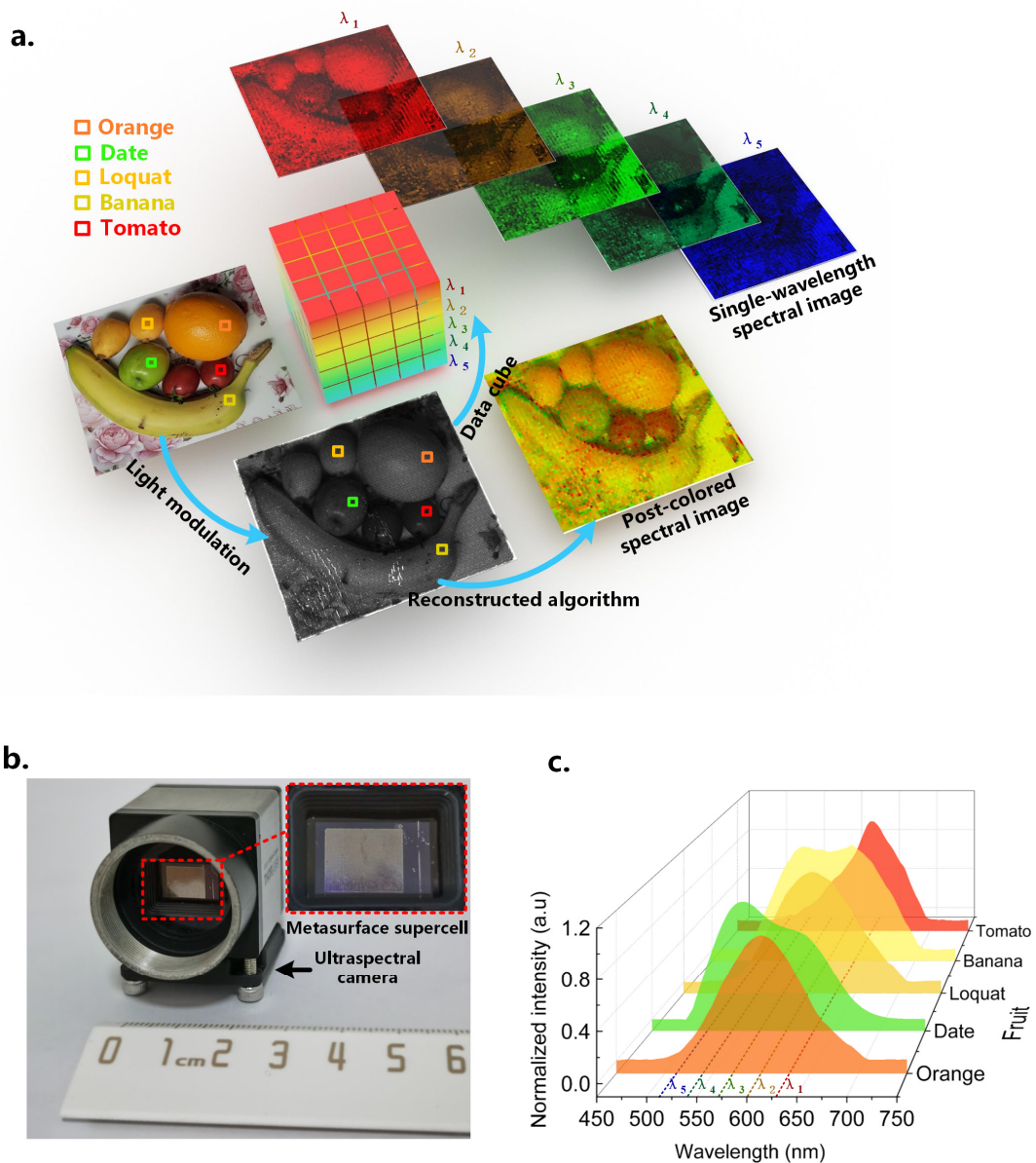


Figure 4 a, Photos of fruits captured using an ordinary color camera and our ultraspectral camera (black-and-white). The black-and-white photo was captured under light of ordinary fluorescent lamps. A post-colored spectral image and a data cube with 601 bands and 6336 spectral pixels are computationally reconstructed from the spectral imaging data, wherein five single-wavelength spectral images are selected from the 601 bands and presented as well. Here, the post-colored spectral image is reconstructed based on the Commission Internationale de l’Eclairage (CIE) 1931 color space³¹. **b**, Ultraspectral camera with a reconfigurable metasurface supercell on the top of CIS. **c**, Spectrum reconstructions with $N = 25$ in five regions of different fruits, orange, date, loquat, banana, and tomato.

In conclusion, we proposed and demonstrated snapshot ultraspectral imaging based on a reconfigurable metasurface supercell. An adaptive strategy determining the spectral bands and spatial units can balance conflicting requirements of spectral width, pixel density, and reconstruction accuracy. It is noteworthy that not only are micro-spectrometers with a high center-wavelength accuracy of 0.04-nm standard deviation and spectral resolution of 0.8 nm realized within a broad wavelength range of 300 nm (450–750 nm), but also by integrating 6336 micro-spectrometers, a snapshot ultraspectral camera with $\Delta\lambda/\lambda\sim 0.001$ is demonstrated. Furthermore, the C_4 symmetric design for the metasurfaces guarantees the polarization independence of the proposed device. Moreover, seamless integration of the reconfigurable metasurface supercell with commercial cameras avoids system incompatibility issues and enables real-time dynamic measurement. Thus, the demonstrated one-shot ultraspectral imaging with both high spectral and spatial resolutions can provide a real-time, dynamic, and high-performance solution for various spectral imaging applications and even a brand-new prospect combining with image recognition and intellisense.

Data and materials availability: The data that were used for the plots in this manuscript and to support other findings are available from the corresponding authors upon reasonable request. In addition, custom code used in this study is available from the corresponding authors upon reasonable request.

Acknowledgments: The authors would like to thank Dr. Di Qu and Mr. Guoren Bai of Tianjin H-Chip Technology Group Corporation, Innovation Center of Advanced Optoelectronic Chip and Institute for Electronics and Information Technology in Tianjin, Tsinghua University for their fabrication support with SEM and ICP etching. This work was supported by the National Key R&D Program of China (Contract Nos. 2018YFB2200402 and 2017YFA0303700); National Natural Science Foundation of China (Grant No. 91750206, 61775115, 61875101); Beijing National Science Foundation (Contract No. Z180012); Tsinghua University Initiative Scientific Research Program; Beijing Innovation Center for Future Chips, Tsinghua University;

Beijing Frontier Science Center for Quantum Information; and Beijing Academy of Quantum Information Sciences.

Author contributions: X.C., J.X., and K.C. contributed equally to this work. X.C. proposed and evaluated the characteristics of micro-spectrometers. K.C. conceived the study and proposed the spectral imaging strategy. J.X. designed metasurface structures and conducted the spectral imaging experiments. Y.H. supervised the project and advised on device optimization. J.X., K.C., and Y.H. wrote the manuscript with contributions from all other coauthors. H.Z. and Z.Z. participated in fabrication. S.X. and Y.H. participated in algorithm optimization. F.L., X.F., and W.Z. provided useful commentary on results. All authors read and approved the manuscript.

References

1. Savage, N. Spectrometers. *Nat. Photonics* **3**, 601 (2009).
2. Bao, J. & Bawendi, M. G. A colloidal quantum dot spectrometer. *Nature* **523**, 67-70 (2015).
3. Yang, Z. *et al.* Single-nanowire spectrometers. *Science* **365**, 1017–1020 (2019).
4. Hagen, N. & Kudenov, M. W. Review of snapshot spectral imaging technologies. *Opt. Eng.* **52**, 090901 (2013).
5. Davis, C. O. Applications of hyperspectral imaging in the coastal ocean. *Imaging Spectrom. VIII* **4816**, 33 (2002).
6. Saral, E., Tun, E. & Gungor, O. Mineral exploration with hyperspectral image fusion. *Signal Processing and Communications Applications Conference (SIU)*, 1281-1284 (2016).
7. Champagne, C., Shang, J., McNairn, H. & Fiset, T. Exploiting spectral variation from crop phenology for agricultural land-use classification. *Remote Sens. Model. Ecosyst. Sustain. II* **5884**, 588405 (2005).
8. He, Z., Shu, R. & Wang, J. Imaging spectrometer based on AOTF and its prospects in deep-space exploration application. *Proc. SPIE* **8196**, 819625 (2011).
9. Schaeppman, M. E. *et al.* APEX: Current status of the airborne dispersive pushbroom imaging spectrometer. *Proc. SPIE* **5234**, 202-210 (2004).

10. Mouroulis, P., Green, R. O. & Chrien, T. G. Design of pushbroom imaging spectrometers for optimum recovery of spectroscopic and spatial information. *Appl. Opt.* **39**, 2210–2220 (2000).
11. Mouroulis, P. & McKerns, M. Pushbroom imaging spectrometer with high spectroscopic data fidelity: experimental demonstration. *Opt. Eng.* **39**, 808-816 (1999).
12. Antila, J. *et al.* Spectral imaging device based on a tuneable MEMS Fabry-Perot interferometer. *Proc. SPIE* **8374**, 83740F (2012).
13. Atherton, P. D., Reay, N. K., Ring, J. & Hicks, T. R. Tunable fabry-perot filters. *Opt. Eng.* **20**, 206806 (1981).
14. Gupta, N. Hyperspectral imager development at army research laboratory. *Infrared Technology and Applications XXXIV* **6940**, 69401P (2008).
15. Vasiliev, A. *et al.* On-chip mid-infrared photothermal spectroscopy using suspended silicon-on-insulator microring resonators. *ACS Sensors* **1**, 1301–1307 (2016).
16. Nitkowski, A., Chen, L. & Lipson, M. Cavity-enhanced on-chip absorption spectroscopy using microring resonators. *Opt. Express* **16**, 11930–11936 (2008).
17. Chen, Y., Lin, H., Hu, J. & Li, M. Heterogeneously integrated silicon photonics for the mid-infrared and spectroscopic sensing. *ACS Nano* **8**, 6955–6961 (2014).
18. Zobenica, Ž. *et al.* Integrated nano-opto-electro-mechanical sensor for spectrometry and nanometrology. *Nat. Commun.* **8**, 1–8 (2017).
19. Gan, X., Pervez, N., Kymissis, I., Hatami, F. & Englund, D. A high-resolution spectrometer based on a compact planar two dimensional photonic crystal cavity array. *Appl. Phys. Lett.* **100**, 231104 (2012).
20. Yesilkoy, F. *et al.* Ultrasensitive hyperspectral imaging and biodetection enabled by dielectric metasurfaces. *Nat. Photonics* **13**, 390-396 (2019).
21. Tittl, A. *et al.* Imaging-based molecular barcoding with pixelated dielectric metasurfaces. *Science* **1109**, 1105–1109 (2018).
22. Faraji-Dana, M. *et al.* Hyperspectral Imager with Folded Metasurface Optics. *ACS Photonics* **6**, 2161–2167 (2019).
23. Wang, Z. *et al.* Single-shot on-chip spectral sensors based on photonic crystal slabs. *Nat. Commun.* **10**, 1–6 (2019).
24. Zhu, Y., Lei, X., Wang, K. X. & Yu, Z. Compact CMOS spectral sensor for the visible spectrum. *Photonics Res.* **7**, 961-966 (2019).
25. Redding, B., Liew, S. F., Sarma, R. & Cao, H. Compact spectrometer based on

- a disordered photonic chip. *Nat. Photonics* **7**, 746–751 (2013).
26. Kurokawa, U., Choi, B. Il & Chang, C.-C. Filter-based miniature spectrometers: spectrum reconstruction using adaptive regularization. *IEEE Sens. J.* **11**, 1556–1563 (2010).
 27. Wang, P. & Menon, R. Computational spectrometer based on a broadband diffractive optic. *Opt. Express* **22**, 14575–14587 (2014).
 28. Chang, C.-C., Lin, N.-T., Kurokawa, U. & Choi, B. Il. Spectrum reconstruction for filter-array spectrum sensor from sparse template selection. *Opt. Eng.* **50**, 114402 (2011).
 29. Oliver, J., Lee, W., Park, S. & Lee, H.-N. Improving resolution of miniature spectrometers by exploiting sparse nature of signals. *Opt. Express* **20**, 2613–2625 (2012).
 30. Zhang, S., Dong, Y., Fu, H., Huang, S. L. & Zhang, L. A spectral reconstruction algorithm of miniature spectrometer based on sparse optimization and dictionary learning. *Sensors (Switzerland)* **18**, 644 (2018).
 31. Broadbent, A. D. A critical review of the development of the CIE1931 RGB color-matching functions. *Color Res. Appl.* **29**, 267–272 (2004).

Supplementary Materials for

One-shot ultraspectral imaging with reconfigurable metasurfaces

S1 Structure design of reconfigurable metasurfaces

In this study, we designed a reconfigurable metasurface supercell composed of 158400 metasurface units, wherein 400 metasurface units with different patterns make up a group and 396 groups are arrayed as 18×22 . These 400 types metasurface structures are designed with C_4 -symmetric¹ with three kinds of basic periodic patterns, viz. circular, square, and cross-shaped patterns, by changing their period, size, and orientation to obtain distinctive light transmission characteristics. As examples, 36 measured transmission spectra selected from these 400 types are shown in Fig. S1 and the corresponding parameters are listed in Table S1. Here, the wavelength range is 450–750 nm and sampling interval is 0.5 nm. During the spectral reconstruction of an object, the adjacent metasurface units are dynamically combined into a reconfigurable and independent spectral pixel.

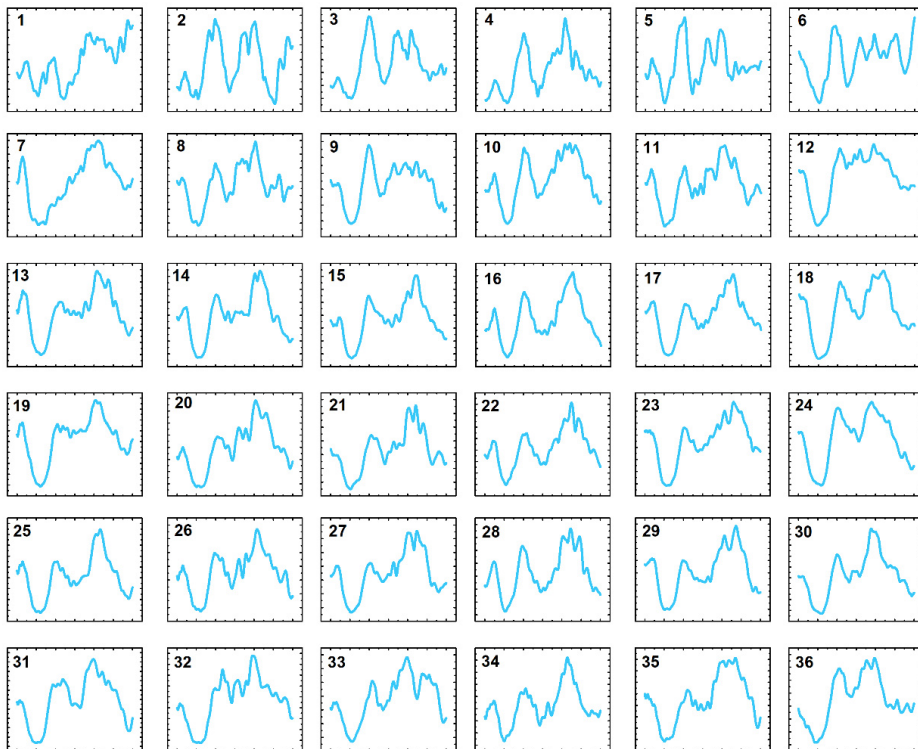


Fig. S1. Measured transmission spectra: 36 spectra selected from 400 types of metasurface structures.

Table S1. Structural parameters for 36 HCGs selected from 400 types of metasurface structures.

STRUCTURE INDEX	HOLE PATTERN	PERIOD (nm)	SIZE PARAMETERS (nm)	ORIENTATION
1	cross	679	long side: 566 short side: 226	45°
2	square	720	square length: 504	0°
3	circle	720	radius: 252	0°
4	square	720	square length: 504	45°
5	cross	720	long side: 548 short side: 219	0°
6	cross	720	long side: 548 short side: 219	45°
7	cross	330	long side: 227 short side: 91	45°
8	square	371	square length: 210	0°
9	circle	371	radius: 105	0°
10	square	371	square length: 210	45°
11	cross	371	long side: 229 short side: 91	0°
12	cross	371	long side: 229 short side: 91	45°
13	cross	330	long side: 275 short side: 110	45°
14	square	371	square length: 260	0°
15	circle	371	radius: 130	0°
16	square	371	square length: 260	45°
17	cross	371	long side: 282 short side: 113	0°
18	cross	371	long side: 282 short side: 113	45°
19	cross	412	long side: 284 short side: 114	45°
20	square	453	square length: 257	0°

21	circle	453	radius: 128	0°
22	square	453	square length: 257	45°
23	cross	453	long side: 279 short side: 112	0°
24	cross	453	long side: 279 short side: 112	45°
25	cross	412	long side: 343 short side: 137	45°
26	square	453	square length: 317	0°
27	circle	453	radius: 159	0°
28	square	453	square length: 317	45°
29	cross	453	long side: 345 short side: 138	0°
30	cross	453	long side: 345 short side: 138	45°
31	cross	494	long side: 340 short side: 136	45°
32	square	535	square length: 303	0°
33	circle	535	radius: 152	0°
34	square	535	square length: 303	45°
35	cross	535	long side: 330 short side: 132	0°
36	cross	535	long side: 330 short side: 132	45°

S2 Polarization-independent design for metasurface structures

Polarization independence is an important feature for not only micro-spectrometers, but also spectral imaging devices, which enables stable operation under various complex measurement scenarios. In addition, the polarization-independence property allows a device to maximize the power of the incident light in a natural lighting environment; in particular, polarization independence could allow for the retention of at least 50% of the incident light energy, thereby significantly improving the signal-to-noise ratio in the reconstructed spectra. This is especially useful in weak-light detection applications such as biofluorescence measurement².

In this study, to ensure that the proposed ultraspectral imaging device is polarization-independent, metasurface structures have been designed with C4 symmetry¹. The transmission spectra of the C4-symmetry metasurface structures with two mutually perpendicular incident polarized beams are simulated using the finite difference time domain (FDTD) method; these spectra are shown in Fig. S2. In this figure, completely consistent transmission spectra corresponding to the two polarization directions indicate the insensitivity of the device to the polarization direction of the incident light.

Furthermore, for specialized requirements of polarized detection, such as in the measurement of Raman spectra, the proposed spectra imaging device can be easily modified by adding extra polarizers.

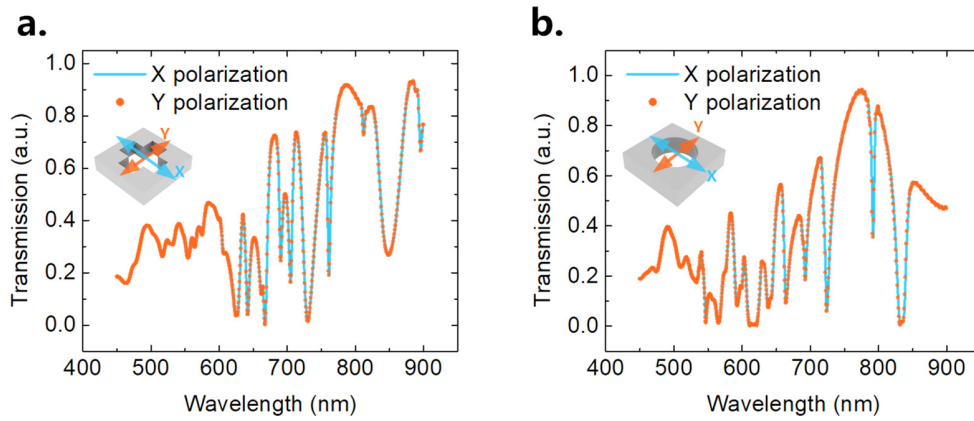


Fig. S2. Simulated transmission spectra of the 2D C₄-symmetry metasurface structure with a **(a)** cross hole (period: 600 nm, long side: 500 nm, short side: 200 nm, thickness: 220 nm) and **(b)** circular hole (period: 540 nm, radius: 180 nm, thickness: 220 nm).

S3 Fabrication of the ultraspectral imaging device

Our fabricated ultraspectral imaging device is based on a reconfigurable metasurface supercell consisting of 158400 metasurface units integrated on top of a CMOS image sensor (CIS) chip. By dynamically defining 25 metasurface units as a single pixel (micro-spectrometer) with size of $80\ \mu\text{m} \times 80\ \mu\text{m}$, a spectral pixel density of $88 \times 72 = 6636$ and size of $7.74\ \text{mm} \times 6.33\ \text{mm}$ ($\approx 0.5\ \text{cm}^2$) are realized.

Here, the reconfigurable metasurface supercell is fabricated on the top of a 220-nm silicon layer of a silicon-on-insulator (SOI) wafer. Fig. S3 shows the fabrication process in detail, which is described as follows:

- 1) Clean the SOI wafer and spin-coat the electron beam photoresist on the top of the SOI wafer.
- 2) Form the metasurface pattern on the photoresist via electron beam lithography.
- 3) Perform inductively coupled plasma (ICP) etching, transfer the pattern onto the top silicon layer, and remove the remaining photoresist.
- 4) Use wet etching with buffered hydrofluoric solution in a water bath at a constant temperature of 40 °C for 3 min to remove the silicon dioxide layer under the top silicon layer.
- 5) Prepare the polydimethylsiloxane (PDMS) transfer with a smooth surface and uniform thickness, and adsorb it on the top silicon layer with the metasurface supercell of the SOI chip using viscous force.
- 6) Quickly tear off the PDMS transfer. The viscous force will peel the top silicon layer with the metasurface supercell off from the substrate.

The peeled metasurface supercell closely sticks to the CIS chip and therefore forms the proposed ultraspectral imaging device.

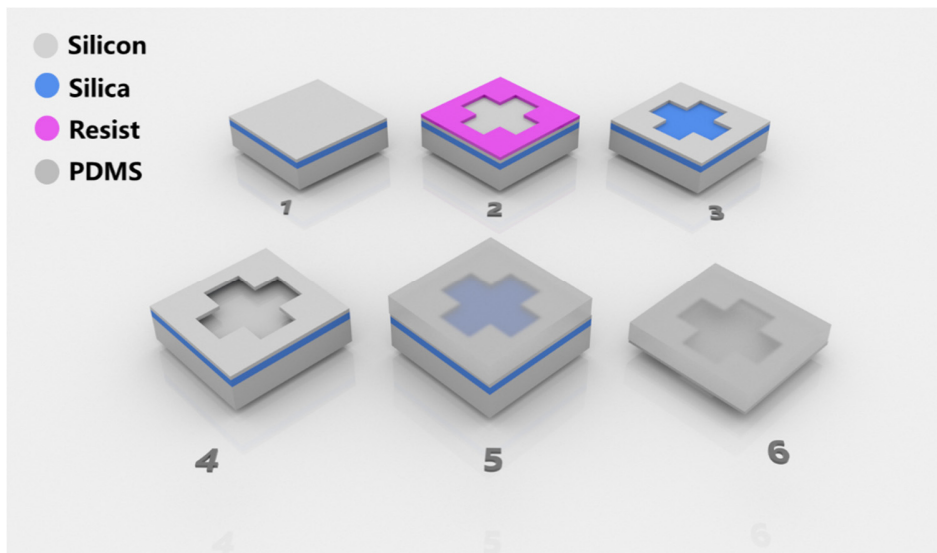


Fig. S3. Fabrication process for the proposed ultraspectral imaging device.

S4 Spectral reconstruction algorithm

The mathematical model for spectral reconstruction has been introduced in Equation (1) and Fig. 1e of the manuscript. The reconstruction of the incident spectrum f is realized by solving the underdetermined system of linear equations with M unknown wavelength points and N measured values:

$$I = Hf \quad (\text{S1})$$

where $I \in R^N$ is the light intensity measured by the CIS, $H \in R^{N \times M}$ is the measurement matrix, and $f \in R^M$ is the incident spectrum to be reconstructed.

In our study, the spectral reconstruction algorithm is realized based on compressive sensing with sparse optimization and dictionary learning^{3,4}. When the spectrum is sparse, such as in the cases of monochromatic light or atomic emission spectra, the linear equations can be solved by optimizing the l_1 -norm minimization problem as follows:

$$\|f\|_1 \text{ subject to } \|Hf - I\|_2 \leq \varepsilon \quad (\text{S2})$$

where the l_1 -norm is defined as $\|f\|_1 = \sum_{i=1}^n |f_i|$ and ε is a positive restriction constant.

When the spectrum is not sparse, which is a common case observed in practice, the spectrum f should first be sparsely represented:

$$f = \Psi s \quad (\text{S3})$$

where $\Psi \in R^{M \times K}$ is the sparse representation matrix and $s \in R^K$ is a sparse vector. The sparse representation matrix Ψ can be obtained via dictionary learning⁵. Then, the reconstruction of the corresponding non-sparse spectrum can be achieved by solving the following optimization problem:

$$\|s\|_1 \text{ subject to } \|H\Psi s - I\|_2 \leq \varepsilon \quad (\text{S4})$$

By obtaining the optimal solution s , the incident spectrum f can be calculated as $f = \Psi s$. Thus far, we have proved that input spectra with varied features (Figs. 2 and 3 in the manuscript) can be reconstructed using this combination of both sparse optimization and dictionary learning.

References:

1. Ikeda, K. et al. Polarization-independent high-index contrast grating and its fabrication tolerances. *Appl. Opt.* **52**, 1049–1053 (2013).
2. Moerner, W. E. & Fromm, D. P. Methods of single-molecule fluorescence spectroscopy and microscopy. *Rev. Sci. Instrum.* **74**, 3597–3619 (2003).
3. Chang, C.-C. Spectrum reconstruction for filter-array spectrum sensor from sparse template selection. *Opt. Eng.* **50**, 059804 (2011).
4. Zhang, S., Dong, Y., Fu H., Huang, S. L. & Zhang, L. A spectral reconstruction algorithm of miniature spectrometer based on sparse optimization and dictionary learning. *Sensors* **18**, 644 (2018).
5. Aharon, M., Elad, M. & Bruckstein, A. K-SVD: An algorithm for designing overcomplete dictionaries for sparse representation. *IEEE Trans. Signal Process.* **54**, 4311–4322 (2006).